The shortwave radiative forcing bias of liquid and ice clouds from MODIS observations

Lazaros Oreopoulos[1,2], Steven Platnick[2,1], Gang Hong[3], Ping Yang[3], and Robert F. Cahalan[2,1]

1. Joint Center for Earth Systems Technology, University of Maryland Baltimore County, Baltimore, MD

2. Laboratory for Atmospheres, NASA Goddard Space Flight Center, Greenbelt, MD

3. Department of Atmospheric Sciences, Texas A&M University, College Station, TX

Submitted to the J. Climate

July 2008

Corresponding author address:
Lazaros Oreopoulos
NASA-GSFC
Code 613.2
Greenbelt, MD 20771

Abstract

We analyze the plane-parallel bias of the shortwave cloud radiative forcing SWCRF of liquid and ice clouds at 1 deg scales using global MODIS (Terra and Aqua) cloud optical property retrievals for four months of 2005 representative of the meteorological seasons. The (negative) bias is estimated as the difference of the SWCRF calculated using the Plane-Parallel Homogeneous (PPH) method and the Independent Column Approximation (ICA). These calculations require MODIS-derived means (for PPH calculations) and distributions (for ICA calculations) of cloud optical thickness and effective radius as well as ancillary surface albedo and atmospheric information consistent with the MODIS retrievals, that are inserted into a broadband solar radiative transfer code. The absolute value of global SWCRF bias of liquid clouds at the top of the atmosphere is ~6 Wm^{-2} for MODIS overpass times while the SWCRF bias for ice clouds is smaller in absolute terms by ~0.7 Wm^{-2}, but with stronger spatial variability. If effective radius variability is neglected (only optical thickness horizontal variations are accounted for), the absolute SWCRF biases increase by about 0.3-0.4 Wm^{-2} on average. Marine clouds of both phases exhibit greater (more negative) SWCRF biases than continental clouds. Finally, morning (Terra)–afternoon (Aqua) differences in SWCRF bias are much more pronounced for ice than liquid clouds, up to about ~15% (Aqua producing stronger negative bias) on global scales, with virtually all contribution to the difference coming from land areas. The substantial magnitude of the SWCRF bias, which for clouds of both phases is collectively about 4 Wm^{-2} for *diurnal averages*, should be a strong motivation to accelerate efforts that link cloud schemes accounting for subgrid condensate variability with appropriate radiative transfer schemes in global climate models.

1. Introduction

In a recent study Oreopoulos et al. (2007) examined the albedo bias from neglecting the variability of MODIS (Moderate Resolution Imaging Spectroradiometer)-inferred liquid cloud optical thickness and effective radius within 1° regions and using mean values instead. This so called Plane-Parallel Homogeneous (PPH) bias (Cahalan et al., 1994a) assumed values close to 0.03, i.e., about 10% of the liquid cloud albedo calculated with spatial cloud variations included. The motivation behind that study was the lack of an extensive global mapping of the PPH bias, with previous published satellite studies being mainly assessments of the visible PPH bias over limited parts of the globe (Barker 1996, Oreopoulos and Davies 1998; Pincus et al., 1999), or focusing rather on parameters quantifying the underlying cloud horizontal inhomogeneity (Rossow, 2002; Oreopoulos and Cahalan 2005) instead of the broadband bias itself. The current study seeks to expand the Oreopoulos et al. (2007) study by providing better seasonal coverage (using one representative months for each season instead of only winter-summer coverage) and by also including clouds classified by MODIS to be of ice phase (near their top). A newer, improved version of MODIS cloud data is used, and emphasis in placed on the shortwave (SW) Cloud Radiative Forcing (SWCRF) bias which takes into account the areal coverage and frequency of occurrence of the two (liquid and ice) cloud types and relates directly the magnitude of the bias to the radiative energy budget. The SWCRF bias features presented here along with the online collection of PPH albedo biases from ISCCP (International Satellite Cloud Climatology Project) at http://isccp.giss.nasa.gov (from larger reference areas and assuming a different cloud classification of low, middle and high clouds) provides a fairly comprehensive picture of the radiative effects of neglecting horizontal cloud inhomogeneity. Any global models that aspire to produce clouds with known subgrid properties, and super-parameterization approaches (Khairoutdinov et al., 2005) should find these datasets valuable for validation.

The dataset and computational details are provided in the next section; the various dependencies of the global and local SWCRF biases are detailed in the five subsections of section 3, while conclusions, along with suggestions on how to exploit the results for global model validation, are provided in section 4.

2. Dataset and radiative transfer calculations

As in Oreopoulos et al. (2007), we use daily MODIS Level-3 (1° resolution gridded) daytime data from both the Terra (~10:30 local time overpass) and Aqua (~13:30 overpass) satellites (datasets MOD08_D3 and MYD08_D3, respectively). This time we use products from the most recent processing stream, Collection 5, and extend the study to four months, January, April, July, and October 2005. We extract the mean daily values of vertically integrated optical thickness ($\overline{\tau}$), effective radius ($\overline{r_e}$), cloud fraction of successful cloud retrievals (A_c), and solar zenith angle (SZA), as well as one-dimensional (1D) histograms of τ and joint (2D) histograms of τ-r_e and τ-cloud top temperature (T_c), constructed by sampling every 5th pixel of the original 1 km resolution retrieval (King et al., 2003). The 1D histograms of τ are resolved in 45 bins for liquid clouds and 30 bins for ice clouds. The 2D histograms of τ and r_e are resolved in 110 bins (11 for τ covering the range 0.1-100 and 10 for r_e covering the range 3 to 30 μm) for liquid clouds, and 143 bins for ice clouds (11 for τ covering the range 0.1-100 and 13 for r_e covering the range 5 to 90 μm); the joint histograms of τ and T_c are resolved in 143 bins (11 for τ and 13 for T_c) for both phases. Except for high latitudes where gridboxes can be revisited within the same day due to orbital swath overlap, the daily histograms represent instantaneous spatial variability of τ and r_e within the 1°x1° gridbox.

The radiative transfer calculations yielding daily atmospheric column albedo, transmittance, and absorptance are performed with a version of the broadband (BB) SW Column Radiation Model (CORAM) of Chou et al. (1998). The salient features of this code and the manner in which it is interfaced with the MODIS retrievals, Global Data Assimilation System (GDAS) atmospheric information (Derber et al., 1991) and MODIS-derived surface albedo (Moody et al., 2005) is described in Oreopoulos et al. (2007) and Oreopoulos and Platnick (2008). In our radiative transfer calculations, the cloud is placed in the layer whose top temperature is closest to the mean cloud top temperature ($\overline{T}_c$) as derived from the joint histogram of τ and T_c. Since the MODIS-inferred cloud properties are placed in a single layer of our atmospheric profile, there is no need to deal with cloud overlap which is in any case not resolved by the passive MODIS observations.

An important modification in our version of the CORAM is the introduction of a new method of calculating cloud optical properties (extinction, single-scattering albedo, asymmetry factor). The changes implemented for liquid clouds are described in Oreopoulos et al. (2007) and Oreopoulos and Platnick (2008). One of the reasons the original parameterization was changed was to extend its applicable range above the upper limit 20 μm for which it was designed originally, considering that MODIS liquid effective radius retrievals can be as high as 30 μm. The retrieved τ from MODIS was used in the broad ultraviolet-visible (UV-VIS) band of the CORAM which assumes a constant cloud extinction coefficient. The spectral values of τ for the remaining three bands in the SW infrared and near infrared (also with flat extinction coefficients) were found by rescaling the MODIS τ with the ratio of the extinction coefficient for those bands with its counterpart in the UV-VIS band for the appropriate retrieved value of r_e. For ice clouds a new parameterization of scattering properties is used, based on the ice particle single-scattering properties of Yang et al. (2000, 2005). The ice habit distribution is consistent with that used for the MODIS retrieval look-up tables of Collection 5, which come from Baum et al. (2005). The particle size distributions of ice clouds come from several compaigns (see details in Baum et al., 2005) and from 21 of the 30 distributions in Fu (1996). The cloud mass extinction coefficient (β), single scattering co-albedo (1-ϖ) and asymmetry factor (g) are fitted as a function of the effective ice crystal diameter D_e of the particle size distribution as follows:

$$\beta = a_0 + \frac{a_1}{D_e} + \frac{a_2}{D_e^2} \tag{1a}$$

$$1 - \varpi = b_0 + b_1 D_e + b_2 D_e^2 + b_3 D_e^3 + b_4 D_e^4 + b_5 D_e^5 \tag{1b}$$

$$g = \begin{cases} c_0 + c_1 D_e & \text{for } D_e \le 40\,\mu m \text{ and } D_e \ge 200\,\mu m \\ c_0 + c_1 D_e + c_2 D_e^2 + c_3 D_e^3 + c_4 D_e^4 + c_5 D_e^5 & \text{for } 40\ \mu\text{m} < D_e < 200\,\mu m \end{cases} \tag{1c}$$

where the fitting coefficients a_0, a_1, a_2, b_0, b_1, etc., are found from regression. There is one set of cofficients for each SW infrared and near infrared band (i.e, flat single-scattering properties are again asumed for these bands) and 8 sets of coefficients for the UV-VIS band, one for each of its 8 sub-bands. Thus, there are 11 sets of fitting coefficients in total. The ice optical thickness retrieved by MODIS was assigned to sub-band 8 of the model's band 1 which covers the visible spectral range. The spectral optical thicknesses in the remaining model bands were found using the same rescaling procedure described above for liquid clouds.

Similar to Oreopoulos et al. (2007), three different albedos (R) are calculated with the SW code: (1) albedos using the $\overline{\tau}$ and $\overline{r}_e$ values of the gridbox (the PPH albedo R_{PPH}); (2) albedos using the 1D histogram of τ and the gridbox mean value of effective radius $\overline{r}_e$ (type 1 ICA albedo R_{ICA1}), i.e., obtained from multiple albedo calculations weighted by the relative frequency in each τ bin; and (3) albedos using the 2D histogram (type 2 ICA albedo R_{ICA2}), i.e., obtained from multiple albedo calculations weighted by the relative frequency in each (τ, r_e) bin. The albedo calculated from the first method minus that calculated from the second gives the classic plane-parallel albedo bias with constant microphysics ($B_1^R > 0$). The albedo calculated from the first method minus that calculated from the third gives the albedo bias due to horizontal variations of both τ and r_e ($B_2^R > 0$). Mathematically, the biases can be expressed as follows:

$$B_1^R\left(\overline{\tau},\overline{r}_e,\nu_\tau,\mu_0\right) = R_{PPH} - R_{ICA1} \equiv \mathbf{R}\left(\overline{\tau},\overline{r}_e,\mu_0\right) - \int \mathbf{R}\left(\tau,\overline{r}_e,\mu_0\right)p(\tau)d\tau \qquad \text{(2a)}$$

$$B_2^R\left(\overline{\tau},\overline{r}_e,\nu_{\tau,r_e}\mu_0\right) = R_{PPH} - R_{ICA2} \equiv \mathbf{R}\left(\overline{\tau},\overline{r}_e,\mu_0\right) - \int\int \mathbf{R}\left(\tau,r_e,\mu_0\right)p(\tau,r_e)d\tau dr_e \qquad \text{(2b)}$$

where μ_0 is the cosine of the solar zenith angle, ν is a measure of either τ or joint τ-r_e variability (e.g., a shape parameter of the 1-D probability density function $p(\tau)$ or the 2-D probability density function $p(\tau, r_\mathrm{e})$), and **R** is the reflectance function (e.g., the analytical solution of the two-stream approximation). The dependencies of the albedo bias on molecular absorption, Rayleigh scattering, and surface albedo are not explicitly shown in the above equations, so Eqs. (2a) and (2b) strictly refer to isolated clouds only. It should be understood, however, that all these factors (assumed to be homogeneous within the 1° gridbox) are accounted for in our calculations. Note that the ICA calculations are subject to errors due to the discretization of the 1D and 2D histograms, but these errors are of random nature. Still, they may result in occasional negative values of bias which are set back to zero whenever they occur. Since ICA albedos are based on 1D radiative transfer calculations, they also suffer, of course, from errors due to neglect of real-world horizontal photon transfer (e.g., Cahalan et al., 1994b).

Oreopoulos et al. (2007) has shown that the albedo bias and the bias in the top-of-the-atmosphere (TOA) shortwave cloud radiative forcing $\Delta SWCRF^{\mathrm{TOA}}$ are simply related via:

$$\Delta SWCRF^{TOA}(<0) \equiv SWCRF_{PPH}^{TOA} - SWCRF_{ICA}^{TOA} = -A_c B^R \mu_0 S_0 \tag{3}$$

where $SWCRF^{TOA}$ is simply defined as the difference in reflected solar fluxes between cloudless and all-sky (i.e., including clear-cloud mixtures) conditions (Ramanathan et al., 1989), μ_0 is the cosine of the solar zenith angle, and S_0 is the incident solar irradiance at TOA. Note that since $B^R > 0$, $\Delta SWCRF^{TOA}$ is a negative quantity that requires no separate estimations of the individual PPH and ICA SWCRFs because the cloudless sky fluxes are identical and cancel out. With all forcing calculations refering to TOA in this paper, the particular superscript will be dropped for simplicity. Moreover, the negative sign of the SWCRF bias is also dropped and all magnitude comparisons are discussed in terms of absolute values.

The SWCRF bias estimates are performed for each day of the month in each gridbox where illumination conditions allow MODIS cloud property retrievals, and are then arithmetically averaged to monthly values (the impact of some averaging choices is examined later). Zonal and global averages of the gridpoint monthly values are trivially estimated as in Oreopoulos et al. (2007), but with gridpoints not receiving solar illumination contributing zero to the averages. Except for subsection 3e where we explicitly examine Terra-Aqua differences, all other results presented are averages from the two satellites.

3. Results

a. Overpass vs. daily and diurnal SWCRF bias

The simplest calculation of Δ*SWCRF* for a particular day involves combining the Terra and Aqua PPH albedo bias B^R with the insolation corresponding to the gridbox mean SZA for that day as extracted from the MOD08_D3 and MYD08_D3 files. This SZA for most gridpoints corresponds to the SZA of the only daylight overpass for that day and is thus ~ 90 min removed from the SZA at local noon. We call the SWCRF bias obtained this way "overpass" Δ*SWCRF*. Since it corresponds to relatively high sun conditions it does not portray accurately the true energy impact of the neglect of horizontal cloud inhomogeneity for the duration of the entire day (sunrise to sunset). An accurate, true diurnal estimate of Δ*SWCRF* is on the other hand not possible since the diurnal variation of cloud properties (cloud fraction and cloud properties that determine their albedo) is not properly resolved with only the two measurements available within daytime. To be able to assess, however, even crudely the influence of variable solar illimination throughout the day, we adopt the methodology of Oreopoulos et al. (2007) for calculating "daytime" Δ*SWCRF*'s, i.e., we pair the instantaneous PPH albedo with the instantaneous insolation at 2-hour intervals, and integrate over the points in time when the sun is above the horizon. For the time period between sunrise and noon the Terra cloud retrievals are used while from noon to sunset Aqua retrievals are used, both assumed constant within their respective daytime half. These calculations of daytime Δ*SWCRF* are significantly more expensive computationally than the overpass Δ*SWCRF* calculations, involving multiple bias calculations per day for each gridbox.

But for the SWCRF biases to be comparable with other biases or forcings that operate uninterrupted (e.g., counterpart infrared CRF biases due to neglect of horizontal cloud condensate or cloud-top temperature variations), even the daytime $\Delta SWCRF's$ are not proper measures of the energetic impact of cloud inomogeneities. Rather 24-h (“diurnal”) estimate of the SWCRF biases are needed, and those can be obtained (again, as in Oreopoulos et al., 2007) by scaling the daytime biases further down by the fraction of the 24-h period that the sun is above the horizon for each gridpoint.

The mean Terra-Aqua global biases of all three types of $\Delta SWCRF$ due to the combined optical thickness and effective radius horizontal variability (i.e., B_2^R used in Eq. 3) are shown in stack-bar graph form in Fig. 1. The values in parentheses indicate the ratio of global mean to standard deviation for the overpass case. The ice cloud $\Delta SWCRF$ is more spatially variable than that of liquid clouds and there is a slight but distinct tendency of greater dispersion for the vernal and autumnal months compared to the winter and summer months. Due to the seasonal changes in the geographical distribution of the SWCRF bias, the latitudinal dependence of daytime length, and the non-linear nature of the global calculation, an empirical conversion of global overpass bias to global daytime or diurnal bias does not exist: the ratio of daytime to overpass global bias ranges from ~0.65 to 0.78, while the ratio of diurnal to overpass global bias spans an approximate 0.32 to 0.42 range. These values are similar to those of Oreopoulos et al. (2007) for liquid clouds.

Overall, liquid clouds exhibit larger $\Delta SWCRF$ than ice clouds (~6.1 vs. 5.4 Wm^{-2} for overpass bias), with the largest disparity in January (> 1 Wm^{-2} for overpass bias) and the smallest in April (< 0.25 Wm^{-2} for overpass bias, increasing interestingly to about 0.5 Wm^{-2} for daytime bias). The seasonal variability of bias is relatively stronger for liquid than for ice clouds, especially for daytime and diurnal averages. Further analysis liquid/ice $\Delta SWCRF$ contrasts is presented in subsection 3c where cloud fraction and frequency of occurrence contributions to the bias are discussed.

b. SWCRF bias with and without r_e variability

As explained in Oreopoulos et al. (2007) for liquid clouds, inclusion of r_{e} horizontal variability in addition to τ variability, reduces $\Delta SWCRF$ because of the negative contribution to the PPH bias stemming from the weak concavity of the albedo vs. r_{e} curve under constant τ. Essentially, once τ variability is specified from the combined τ-r_{e} MODIS retrievals, the r_{e} spatial variability is only generating asymmetry factor and single-scattering albedo variability. A similar influence also exists for ice clouds. Figure 2 contrasts liquid and ice clouds in terms of the global $\Delta SWCRF$ reduction arising from r_{e} spatial variability contributions, i.e., $\left|A_c(B_1^R - B_2^R)\mu_0 S_0\right|$. The global effect of r_{e} spatial variability is a reduction of the combined Terra-Aqua absolute value of the overpass bias by about 0.4 $\mathrm{Wm^{-2}}$ (~ 7%) for liquid clouds and about 0.25 $\mathrm{Wm^{-2}}$ (~ 5%) for ice clouds. Other than this, there are no major impacts in the qualitative behavior of $\Delta SWCRF$ by neglecting r_e horizontal inhomogeneity in the calculations. For example, the ratio of global mean to standard deviation decreases only very slightly when r_e variability is neglected suggesting only minor effects in the spatial patterns of the $\Delta SWCRF$ distribution. Henceforth, all SWCRF bias results will be B_2^R-based.

c. Cloud fraction and frequency of occurrence contributions to monthly SWCRF bias

Equation (3) clearly indicates that the daily SWCRF bias of a gridpoint depends on three factors: (1) the PPH albedo bias B^R of the cloudy portion of the gridpoint; (2) the cloud fraction A_c, and (3) the solar irradiance $\mu_0 S_0$ received by the gridpoint. Upon dividing $\Delta SWCRF$ by A_c, the forcing bias becomes the bias of the reflected TOA flux for the cloudy portion of the gridpoint. For a given incident solar flux, this allows to examine whether high (low) Δ*SWCRF's* come from high (low) PPH albedo biases or high (low) cloud fractions or a combination of both. Here, we identify these "per unit cloud fraction" SWCRF biases as "no CF" biases, as in "no cloud fraction was accounted for in the calculation".

Furthermore, when calculating a gridpoint's monthly mean SWCRF bias, averaging can be performed either over the number of days when a cloud of a particular phase was encountered during an overpass, making such an observation possible, or over the total number of days within the month with an overpass. The latter calculation thus assigns zero contributions to the monthly Δ*SWCRF* from days where no cloud of the particular phase was observed. If, for example, for a gridpoint with 25 possible observations within a month, only 14 of those had liquid cloud and therefore allowed estimates of liquid SWCRF bias, a monthly value of ΔSWCRF can be obtained by dividing either by 25 or by 14, with the latter calculation reflecting the monthly SWCRF bias of liquid clouds for that gridpoint "when present". This method of not accounting for the frequency of occurrence (FO) of clouds, which obviously gives higher monthly values of Δ*SWCRF,* was used by Oreopoulos et al. (2007) and is identified here as the "no FO" method for calculating monthly values of SWCRF bias. Our default choice in this paper (used for the results shown so far and all the results that follow, unless specifically stated otherwise) of including the zero contributions of days without clouds of a particular phase gives a fairer estimate of monthly SWCRF biases, since the ultimate impact of a forcing (and thererefore its bias) depends on its frequency of occurence. Finally, one may also be interested in the mean SWCRF bias of the cloudy portion of the gridpoint only for those days when cloud was present in the gridpoint. We call this the "no CF/no FO" SWCRF bias because neither cloud fraction nor frequency of occurrence is accounted for. Such a "SWCRF bias" is more closely associated with the fundamental cloud inhomogeneity properties that give rise to the plane-parallel albedo bias.

The global values of all the above types of monthly $\Delta SWCRF$ are compared in the stack bar plot of Fig. 3. The white bars are correspond to the same overpass values shown in Figure 1. Cloud fraction and method of monthly averaging have distinctly different impact on liquid and ice clouds. For instance, if averaging is performed only over the days of the month with clouds of a particular phase present within the gridpoint, the sign of the liquid-ice $\Delta SWCRF$ difference is reversed with ice clouds now having greater biases than liquid clouds (black "CF/no FO" bars). This means that, when present, ice clouds give overall larger biases than liquid clouds, partly due to larger cloud fraction as will be explained shortly, but their overall monthly $\Delta SWCRF$ is reduced because they occur less frequently. When cloud frequency of occurrence is accounted for (averaging over all days of the month with possible observations), but the bias is normalized by the cloud fraction, i.e., when the reflected flux bias of the cloudy portion is examined, the dominance of liquid over ice SWCRF bias is restored and widened (gray "no CF/FO" bars). Evidently, liquid clouds form more frequently (at the time of the satellite overpass at least) and are more inhomogeneous (more accurately: produce large PPH cloud albedo bias) when present. When neither days devoid of clouds of a particular phase nor the cloud fraction is accounted for in monthly estimates $\Delta SWCRF$ (striped "no CF/no FO" bars), the disparity of liquid and ice cloud tapers again because the larger frequency of occurrence of liquid clouds no longer contributes to the monthly bias; nevertheless, overall, the reflected flux bias in areas covered by liquid clouds exceeds that in ice cloud-covered areas, and this is more prominent in January and least in July.

d. Geographical distributions of the SWCRF bias

Figure 4 shows the geographical distribution of liquid and ice cloud overpass SWCRF bias from combined Terra-Aqua results for all four months. The figures reflect known patterns and regimes of the clouds of each phase and have obvious correlations with cloud inhomogeneity and PPH albedo bias maps in Oreopoulos and Cahalan (2005) and Oreopoulos et al. (2007), respectively (the latter only for liquid clouds). The largest liquid $\Delta SWCRF$*'s* occur in January in the vicinity of sea of Japan and the Korean peninsula where mid-latitude winter storm systems form, and in the eastern equatorial Pacific extending to the broader Colombia/Equador region, where cloudiness is of convective origin (Figure 4a). Neither of these two regions stands out in the other three months. The marine stratocumulus regions in the eastern parts of the major oceans also exhibit strong seasonality in $\Delta SWCRF$, with October having in general the largest values, coinciding with the seasonal peak in cloud fraction (Oreopoulos and Davies, 1993). Mid-latitude oceans are quasi-permanent areas of large liquid SWRCF bias, but with values that are largely dependent on available solar illumination (contrast January and July southern oceans). The ice $\Delta SWCRF$ maxima on the other hand are more clearly confined in convective areas and follow the movement of the ITCZ (Figure 4b). The mid-latitude $\Delta SWCRF$*'s* of ice clouds generally stay below ~ 15 Wm^{-2} and are mostly smaller than their liquid counterparts, but not by as much as suggested by their color designation which is partly a result of the wider range of the ice cloud colorbar.

The zonal distribution of monthly $\Delta SWCRF$ (Terra-Aqua averages) is shown only for January and July (Figure 5). In this case we chose to show the 24-h biases to capture latitudinal changes in sunlight duration. Features that also stood out in the full geographical distribution are prominent, such as the summer peaks in mid-latitude liquid SWCRF bias which assume values close to 7 Wm^{-2}. The ice $\Delta SWCRF$ peaks are somewhat smaller and appear in the equatorial zone, shifting with the seasonal movement of the ITCZ. Even though plentiful solar illumination is available, minima occur in broad subtropical zones of descending portions of the Hadley cell where deserts and marine stratocumulus regions are prevalent.

Land-ocean global overpass $\Delta SWCRF$ differences are highlighted in Figure 6. The bias is clearly greater over oceans for both cloud types and all months with the exception of July where liquid cloud biases are very similar over land and ocean. The main reason for this seems to be the dramatic decrease of $\Delta SWCRF$ over the southern midlatitude oceans (Fig. 4a), due to the lower winter solar illumination. Peaks of $\Delta SWCRF$ over certain land areas such as over south Asia probably play only minor role in determining this July near-parity of liquid cloud biases. Besides differences in cloud hetreogeneity, cloud fraction, and availability of solar insolation, the overall lower land *SWCRF* bias is probably also partly attributable to the brighter land surfaces which tend to reduce the cloud albedo contribution to the TOA albedo and therefore dampen albedo differences between homogeneous and inhomogeneous clouds.

e. Terra vs. Aqua differences

Figure 7 show the percentage differences (normalized by the combined Terra-Aqua SWCRF bias) of Terra minus Aqua overpass SWCRF biases. Differences are in general negative (Aqua bias greater in absolute value than Terra bias), but this is much more pronounced for ice clouds, suggesting a stronger diurnal cycle with an afternoon increase in cloud inhomogeneity for this type of clouds. Liquid clouds bias differences are either near-zero (April and July) or of opposite sign (January and October). To isolate the morning-afternoon differences in cloud inhomogeneity from cloud fraction and frequency of cloud occurrence effects, the "no CF/no FO (see subsection 3c) overpass Δ*SWCRF* relative differences are also plotted. The latter differences are now always negative for the liquid clouds too. Clearly, cloud fraction and frequency of occurrence reduces morning-afternoon differences due to cloud inhomogeneity alone, i.e., similar to ice clouds, liquid clouds tend also to be more heterogeneous in the afternoon. This is consistent with the cloud inhomogeneity factor results presented by Oreopoulos and Cahalan (2005) and the PPH albedo bias results of Oreopoulos et al. (2007).

Because global means do not necessarily give the complete picture of Terra and Aqua Δ*SWCRF*'s differences, we performed additional analysis on the July 2005 liquid case exhibiting near-zero Δ*SWCRF* difference and the January 2005 ice case exhibiting the greatest negative bias difference. Figure 8 plots frequency distributions of Terra and Aqua Δ*SWCRF* for these cases. It is apparent that the near parity of Terra and Aqua July liquid Δ*SWCRF* is not the result of cancellations from different segments of the bias distribution. The Aqua and Terra bias histograms overlap almost perfectly before starting to diverge only at the rightmost tail of the distribution representing rare occurences of large Δ*SWCRF* values (top panel). On the other hand, for the January ice case histogram divergence starts at higher normalized frequencies (even though the separation point is again around the 20 Wm^{-2} bin as in the liquid case). Aqua forcing biases for this case are not only overall greater, but their distribution is wider as evidenced both by the shape of the histogram and the magnitude of the standard deviation of the bias distribution (given in parentheses) which is about 20% larger than that of Terra.

Finally, we also examined whether ocean-land contrasts exist in the Terra-Aqua Δ*SWCRF* differences. Figure 9 reveals how the global differences of Fig. 7 are ultimately determined. For liquid clouds, Terra Δ*SWCRF* absolute values systematically exceed (fall behind) those of Aqua over ocean (over land); for ice clouds $\Delta SWCRF$ differences are negligible over ocean and quite substantial over land with the latter obviously responsible for the negative global values in Fig. 7. That this behaviour is driven almost exclusively by morning-afternoon differences in cloud inhomogeneity over land and ocean was confirmed by plotting the counterpart of Fig. 9 for "no CF/no FO" $\Delta SWCRF$*'s* (not shown): oceanic differences hovered around zero while continental differences were strongly negative (Aqua $\Delta SWCRF$*'s* larger in absolute magnitude), for clouds of both phases.

4. Summary and conclusions

The global plane-parallel bias of the shortwave cloud radiative forcing SWCRF (also known as the shortwave cloud radiative effect) at 1 deg scales is examined using global MODIS (Terra and Aqua) cloud optical property retrievals for four months of 2005 representative of the meteorological seasons and a broadband shortwave radiative transfer code. The absolute value of the (negative) global SWCRF bias of liquid clouds at the top of the atmosphere is ~6 $\mathrm{Wm^{-2}}$ for MODIS overpass times skewed towards near solar noon conditions, while the SWCRF bias for ice clouds is smaller in absolute terms by ~0.7 $\mathrm{Wm^{-2}}$, but with stronger spatial variability. A significant contributor to liquid cloud SWCRF biases being greater is the higher frequency of occurrence of liquid clouds, which in conjunction with the higher average plane-parallel albedo bias, overcompensate for the higher cloud fraction of ice clouds, when present. If effective radius variability is neglected (only optical thickness horizontal variations are accounted for), SWCRF biases increase in absolute values by about 0.3-0.4 $\mathrm{Wm^{-2}}$ on average. Rough conversions of these biases to daytime and diurnal (24-h) values yield values that are ~25-35 % and ~60-70 % smaller, respectively. Oceanic clouds of both phases assume larger (more negative) SWCRF biases than continental clouds. Finally, morning (Terra)–afternoon (Aqua) differences in SWCRF bias are much more pronounced for ice than liquid clouds, reaching about ~15% (Aqua producing stronger negative bias) on global scales, with almost all contribution to the difference coming from land areas.

If one wants to distill the present analysis to a single representative number of the lower limit of global SWCRF bias, then the diurnal "24 h" values of Fig. 1, corresponding to combined optical thickness and effective radius variability and accounting for both cloud fraction and frequency of occurrence, are appropriate. Taking the arithmetic mean of the four monthly values yields a SWCRF bias is 2.37 Wm^{-2} for liquid clouds and 1.83 Wm^{-2} for ice clouds. Due to the nature of MODIS observations where liquid and ice clouds cover non-overlapping portions of the gridpoint, these numbers must be added. Their total of 4.2 Wm^{-2} serves then as an estimate of the lower bound of global SWCRF bias. Characterizing this as lower bound is justified mainly by the inclusion of zero contributions from cloudless and non-illuminated areas, and to a lesser extent by the omission of the relatively small fraction of clouds classified by MODIS as "mixed" and "undetermined". Still, a more accurate assessment requires knowledge of the full diurnal variation of cloud properties, and perhaps more sophisticated treatments of atmospheric (e.g., accounting for aerosols) and surface albedo effects.

Our global SWCRF bias values, along with the more detailed breakdown of bias behaviour seen in our full suite of results should provide a valuable validation reference for global modeling approaches that are able to generate mesoscale cloud inhomogeneity, provided that some effort is extended to simulate the MODIS worldview. This would ideally entail use of some type of "MODIS simulator" where the most basic characteristics of passive radiometry retrievals, such as presumably unobscured views for low cloud retrievals, vertical integration of optical thickness, and strong dependence of cloud microphysics and phase characterization to near cloud top conditions, are imitated. The temporal and spatial sampling of MODIS should also be properly taken into account. Furthermore, it is important to keep in mind that any calculations of plane-parallel albedo or forcing bias are tied to the spatial scale at which the horizontal variability of cloud properties is considered, so that any global model–MODIS comparison should be performed on identical grids.

Acknowledgements: L. Oreopoulos gratefully acknowledges support from the U.S. Department of Energy, Office of Science, Office of Biological and Environmental Research, Environmental Sciences Division as part of the ARM program under grant DE-FG02-07ER64354. Partial funding to all GSFC authors was also provided by the NASA Radiation Sciences Program.

References

Barker, H. W., 1996: A parameterization for computing grid-averaged solar fluxes for inhomogeneous marine boundary layer clouds, part I: methodology and homogeneous biases. *J. Atmos. Sci.*, **53**, 2289-2303.

Baum, B. A., A. Heymsfield, P. Yang, and S. T. Bedka, 2005: Bulk scattering properties for the remote sensing of ice clouds I: Microphysical data and models. *J. Appl. Meteor.*, **44**, 1885-1895 .

Cahalan, R. F., W. Ridgway, W. J. Wiscombe, T. L. Bell and J. B. Snider, 1994a: The albedo of fractal stratocumulus clouds. *J. Atmos. Sci.*, **51,** 2434-2455.

Cahalan, R. F., W. Ridgway, W. J. Wiscombe, Harshvardhan, and S. Gollmer, 1994b: Independent pixel and Monte Carlo estimates of stratocumulus albedo. *J. Atmos. Sci.*, **51**, 3776-3790.

Chou, M.-D., M. J. Suarez, C.-H. Ho. M. M.-H. Yan, and K.-T. Lee, 1998: Parameterizations for cloud overlapping and shortwave single-scattering properties for use in general circulation and cloud ensemble models. *J. Climate,* **11,** 202-214.

Derber, J. C., D. F. Parrish, and S. J. Lord, 1991: The new global operational analysis system at the National Meteorological Center. *Weath. Forec.*, **6**, 538–547.

Fu, Q., 1996: An accurate parameterization of the solar radiative properties of cirrus clouds for climate models. *J. Climate*, **9**, 2058-2082.

Hu, Y. X., and K. Stamnes, 1993: An accurate parameterization of the radiative properties of water clouds suitable for use in climate models. *J. Climate*, **6**, 728–742.

Khairoutdinov, M., D. A. Randall, and C. DeMott. 2005: Simulations of the Atmospheric General Circulation Using a Cloud-Resolving Model as a Superparameterization of Physical Processes. *J. Atmos. Sci.,* **62**, 2136–2154.

King, M. D., W. P. Menzel, Y. J. Kaufman, D. Tanré, B.-C. Gao, S. Platnick, S. A. Ackerman, L. A. Remer, R. Pincus, and P. A. Hubanks, 2003: Cloud and aerosol properties, precipitable water, and profiles of temperature and water vapor from MODIS. *IEEE Trans. Geosc. Rem. Sens.*, **41**, 442-458.

Moody, E. G., M. D. King, S. Platnick, C. B. Schaaf, and F. Gao, 2005: Spatially complete global spectral surface albedos: Value-added datasets derived from Terra MODIS land products. *IEEE Trans. Geosci. Remote Sens.*, **43**, 144-158.

Oreopoulos, L., and R. Davies, 1993: Statistical dependence of albedo and cloud cover on sea surface temperature for two tropical marine stratocumulus regions. *J. Climate*, **6**, 2434-2447.

Oreopoulos, L., and R. Davies, 1998: Plane parallel albedo biases from satellite observations. Part I: Dependence on resolution and other factors. *J. Climate*, **11**, 919-932.

Oreopoulos, L., and R. F. Cahalan, 2005: Cloud inhomogeneity from MODIS. *J. Climate*, **18**, 5110–5124.

Oreopoulos, L., R. Cahalan, and S. Platnick, 2007: The plane-parallel albedo bias of liquid clouds from MODIS observations. *J. Climate*, **20**, 5114-5125.

Oreopoulos, L., and S. Platnick, 2008: The radiative susceptibility of cloudy atmospheres to droplet number perturbations, 2: Global analysis from MODIS. *J. Geophys. Res.*, in press.

Pincus, R., S. A. McFarlane, and S. A. Klein, 1999: Albedo bias and the horizontal variability of clouds in subtropical marine boundary layers: observations from ships and satellites. *J. Geophys. Res.*, **104**, 6183-6191.

Ramanathan, V, E. Ahmad, R. D. Cess, E. F. Harrison, P. Minnis, B. R. Barkstrom, and D. Hartmann, 1989: Cloud-radiative forcing and climate: Results from the earth radiation budget experiment. **Science**, 243, 57-63.

Rossow, W. B., C. Delo, and B. Cairns, 2002: Implications of the observed mesoscale variations of clouds for the Earth's radiation budget. *J. Climate*, **15**, 557-585.

Yang, P., K. N. Liou, K. Wyser, and D. Mitchell, 2000: Parameterization of the scattering and absorption properties of individual ice crystals. *J. Geophys. Res.*, **105**, 4699-4718.

Yang, P., H. Wei, H.-L. Huang, B. A. Baum, Y. X. Hu, G. W. Kattawar, M. I. Mishchenko, and Q. Fu, 2005: Scattering and absorption property database for nonspherical ice particles in the near- through far-infrared spectral region. *Appl. Opt.*, **44**, 5512-5523.

Figure Captions

Figure 1. Stack-bar plot showing the combined MODIS Terra-Aqua global monthly-averaged SWCRF bias using B_2^R in Eq. (3) for liquid (lower four bars) and ice (upper four bars) clouds for the four months used in this study. Overpass, daytime, and diurnal (24-hour) values are shown (see text). The values in parentheses indicate the ratio of global mean to standard deviation for the overpass case.

Figure 2. Absolute (Wm^{-2}) and percentage reduction of the combined Terra-Aqua global monthly overpass SWCRF bias from using B_2^R (r_e spatial variability included in PPH bias estimates) instead of B_1^R in Eq. (3).

Figure 3. Stack-bar plot showing global monthly B_2^R-based overpass SWCRF biases for our default calculation (black) and for three other methods that ignore cloud fraction and/or frequency of occurrence of clouds of the respective phase (see text for details). As in the previous plots, the values shown here are Terra-Aqua averages.

Figure 4a. Geographical distribution of the combined Terra-Aqua monthly overpass SWCRF bias of liquid clouds from combined optical thickness and effective radius variability for the four months examined in this paper. Black areas indicate no data availability. Clockwise from top: January 2005, April 2005, October 2005, and July 2005.

Figure 4b. As Fig. 4a, but for ice clouds.

Figure 5. Zonal dependence of the combined Terra-Aqua monthly 24-h SWCRF bias (B_2^R-based) for January and July 2005.

Figure 6. Monthly Terra-Aqua combined B_2^R-based overpass SWCRF bias averaged separately over the globe's land and ocean gridpoints.

Figure 7. Percentage difference (normalized by their combined value) of Terra minus Aqua global monthly overpass SWCRF biases (B_2^R-based). Along with the default regular SWCRF biases, results from the "no CF/no FO" (see subsection 3c) bias calculation are also shown. These reveal the extent to which the Terra-Aqua SWCRF biases are due to differences in cloud fraction (CF) and frequency of cloud occurrence (FO).

Figure 8. Logarithmic normalized frequency of occurrence of monthly overpass SWCRF biases (B_2^R-based) for July 2005 liquid clouds (top) and January 2005 ice clouds (bottom). The global mean SWCRF biases and their standard deviations (in parentheses) are also given.

Figure 9. Absolute difference of Terra minus Aqua monthly overpass SWCRF biases (B_2^R-based) averaged separately over the globe's ocean and land gridpoints.

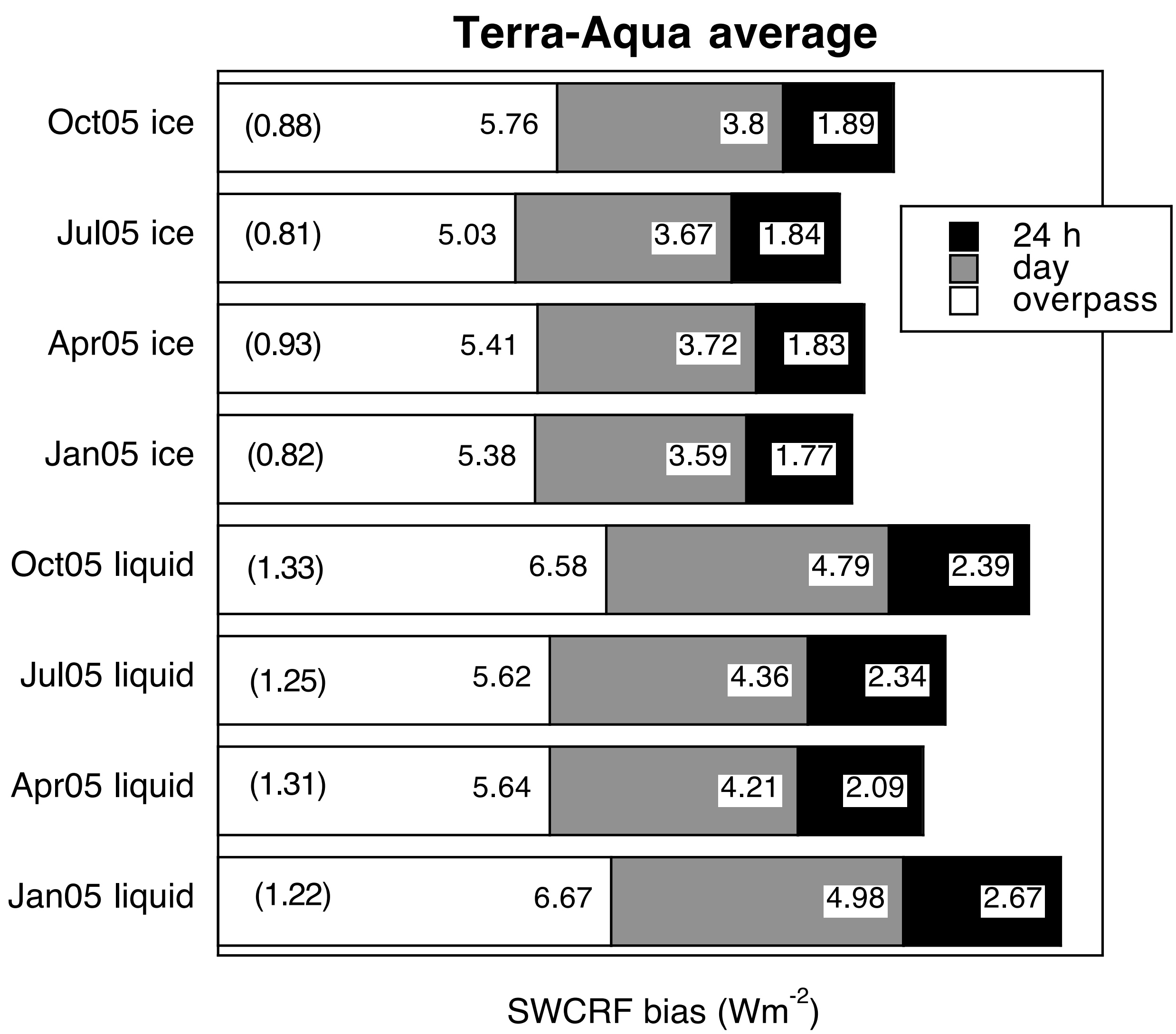

Figure 1. Stack-bar plot showing the combined MODIS Terra-Aqua global monthly-averaged SWCRF bias using B_2^R in Eq. (3) for liquid (lower four bars) and ice (upper four bars) clouds for the four months used in this study. Overpass, daytime, and diurnal (24-hour) values are shown (see text). The values in parentheses indicate the ratio of global mean to standard deviation for the overpass case.

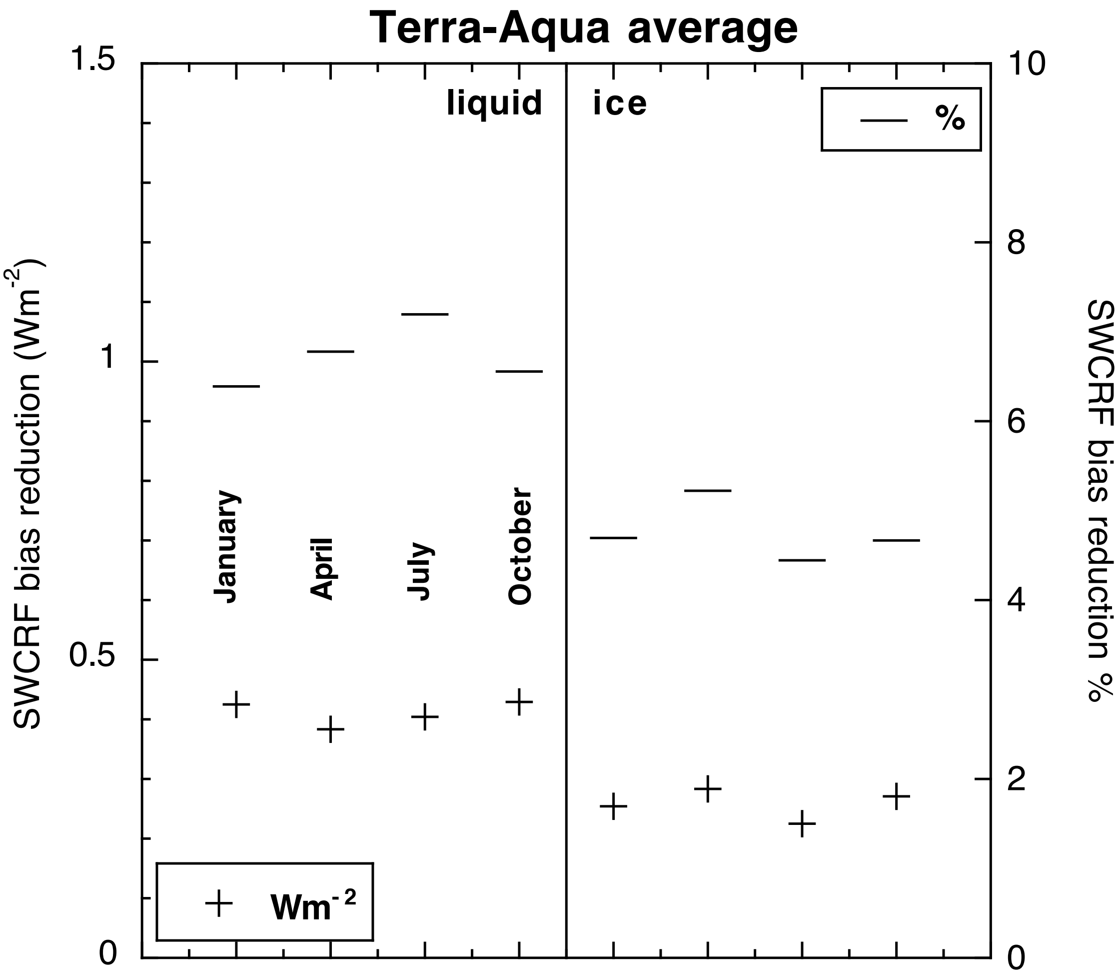

Figure 2. Absolute (Wm^{-2}) and percentage reduction of the combined Terra-Aqua global monthly overpass SWCRF bias from using B_2^R (r_e spatial variability included in PPH bias estimates) instead of B_1^R in Eq. (3).

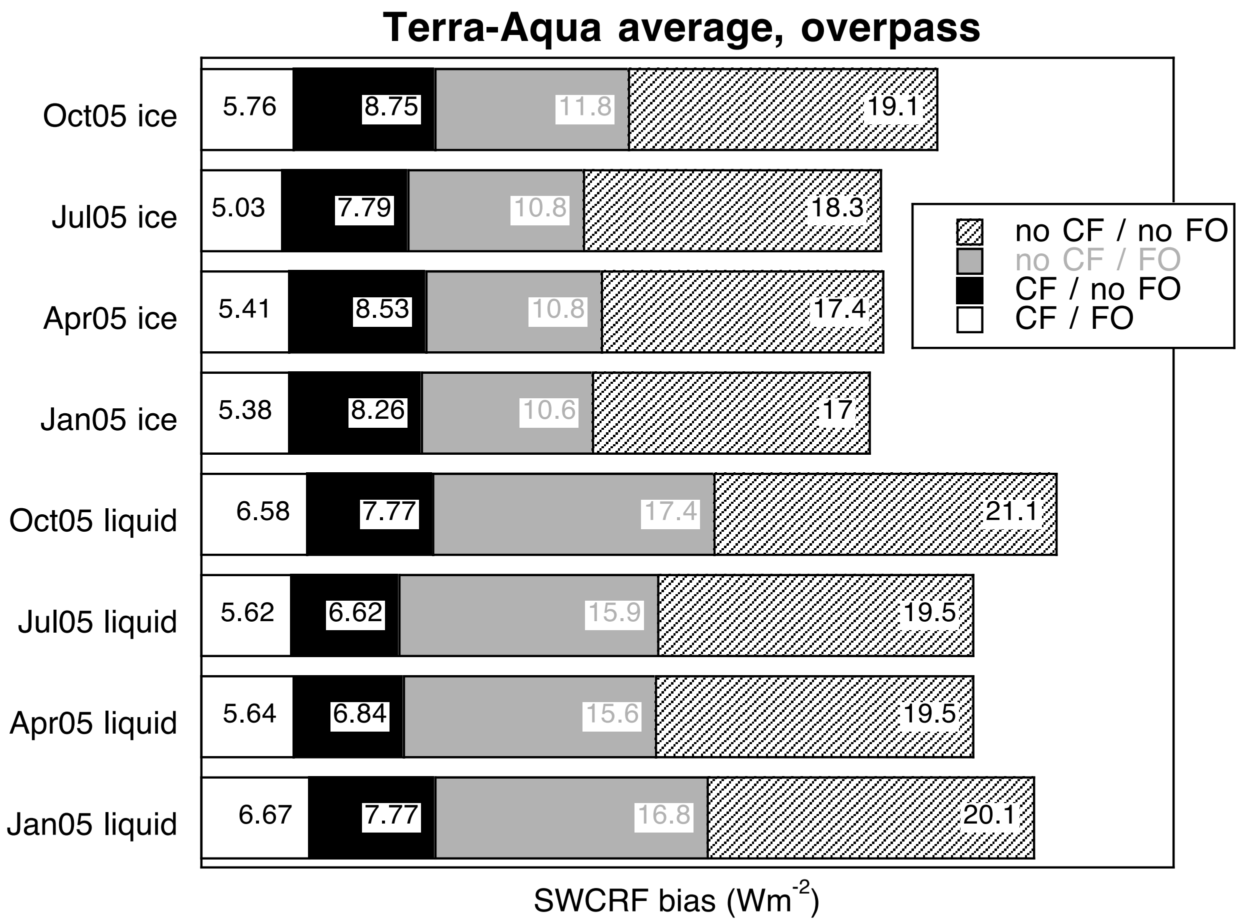

Figure 3. Stack-bar plot showing global monthly B_2^R-based overpass SWCRF biases for our default calculation (black) and for three other methods that ignore cloud fraction and/or frequency of occurrence of clouds of the respective phase (see text for details). As in the previous plots, the values shown here are Terra-Aqua averages.

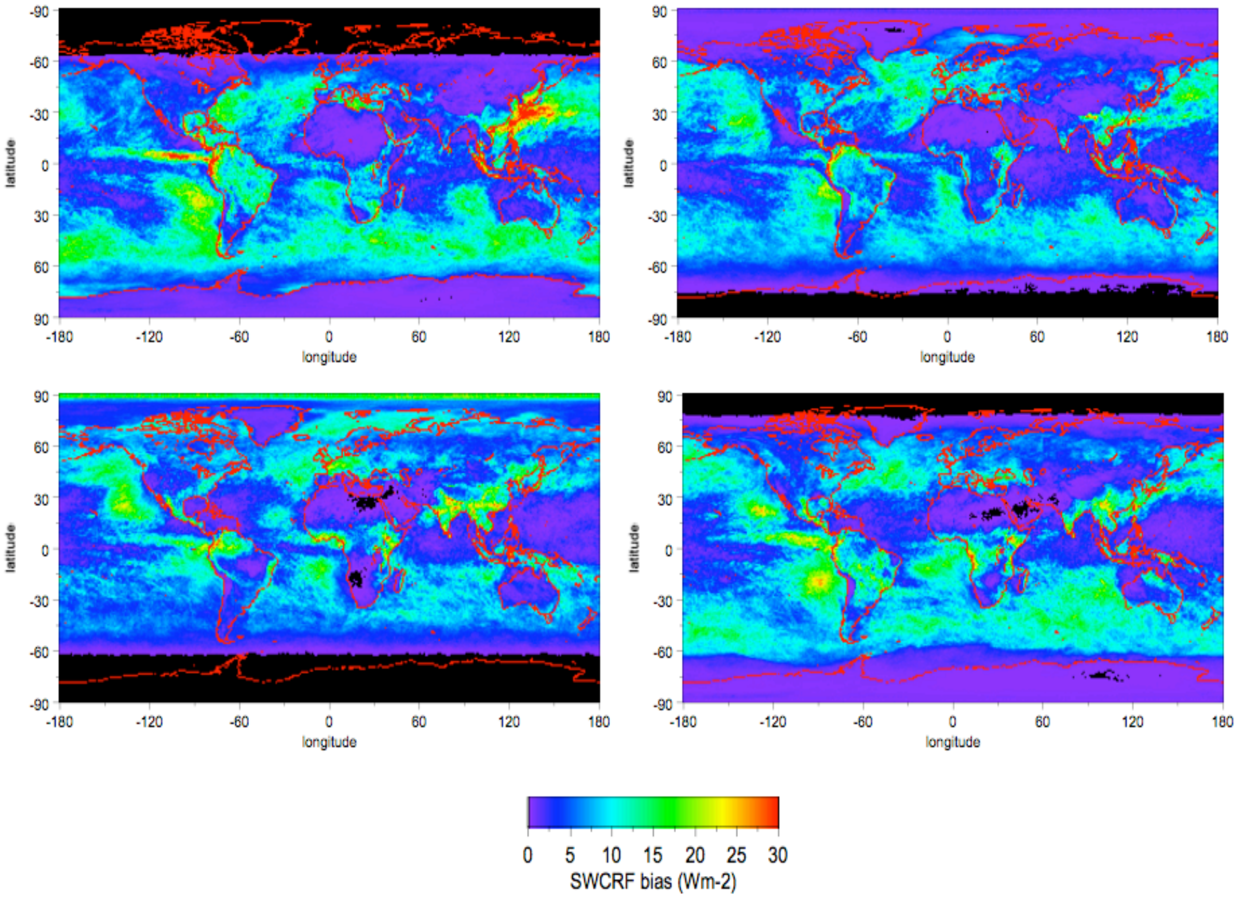

Figure 4a. Geographical distribution of the combined Terra-Aqua monthly overpass SWCRF bias of liquid clouds from combined optical thickness and effective radius variability for the four months examined in this paper. Black areas indicate no data vailability. Clockwise from top: January 2005, April 2005, October 2005, and July 2005.

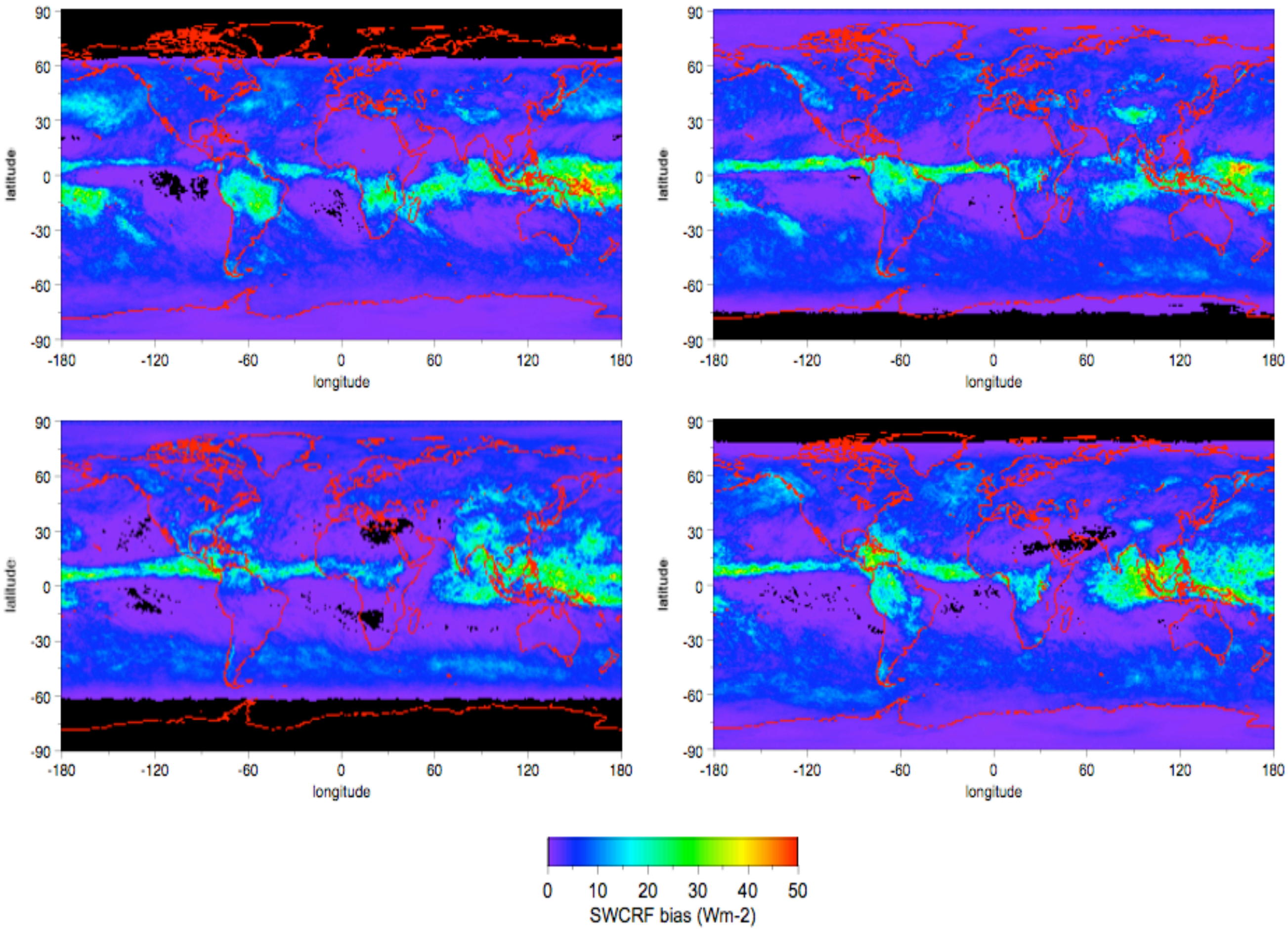

Figure 4b. As Fig. 4a, but for ice clouds.

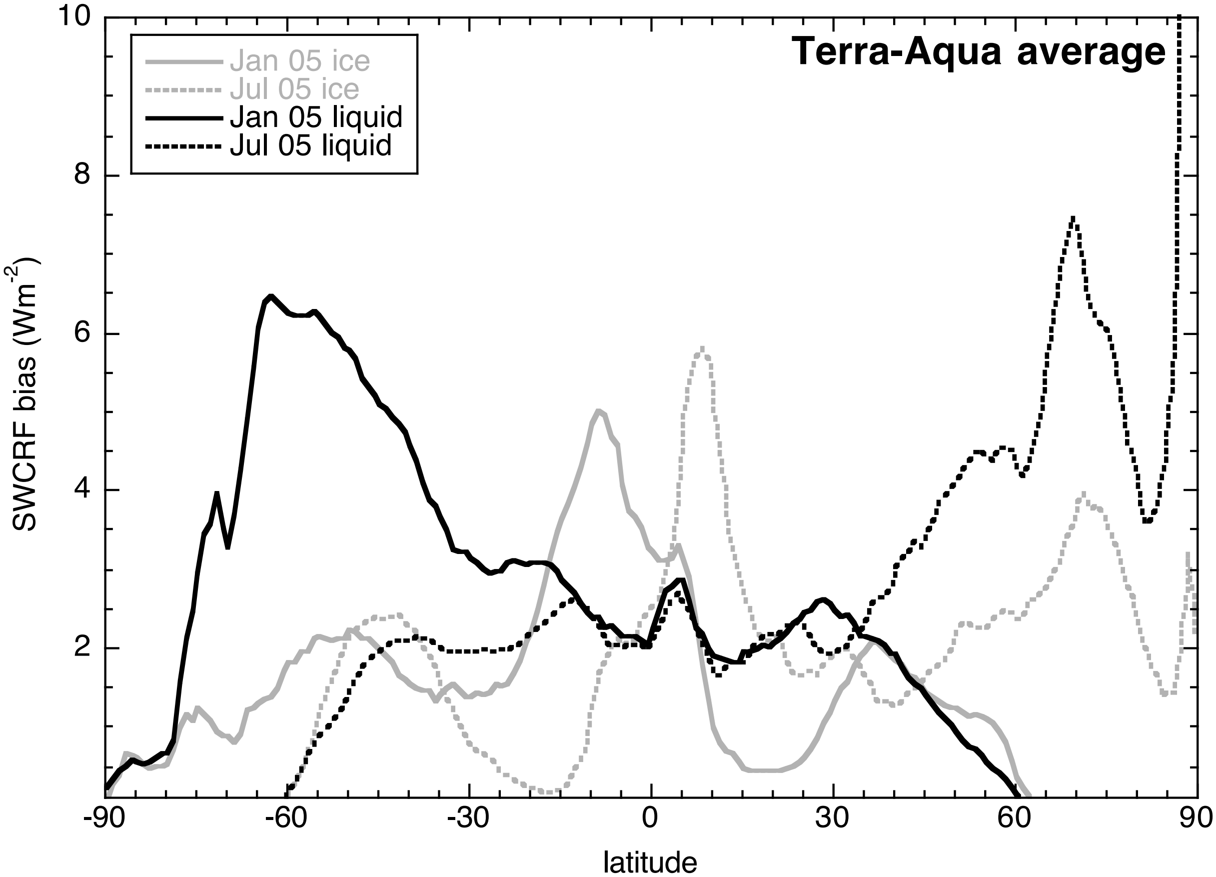

Figure 5. Zonal dependence of the combined Terra-Aqua monthly 24-h SWCRF bias (B_2^R-based) for January and July 2005.

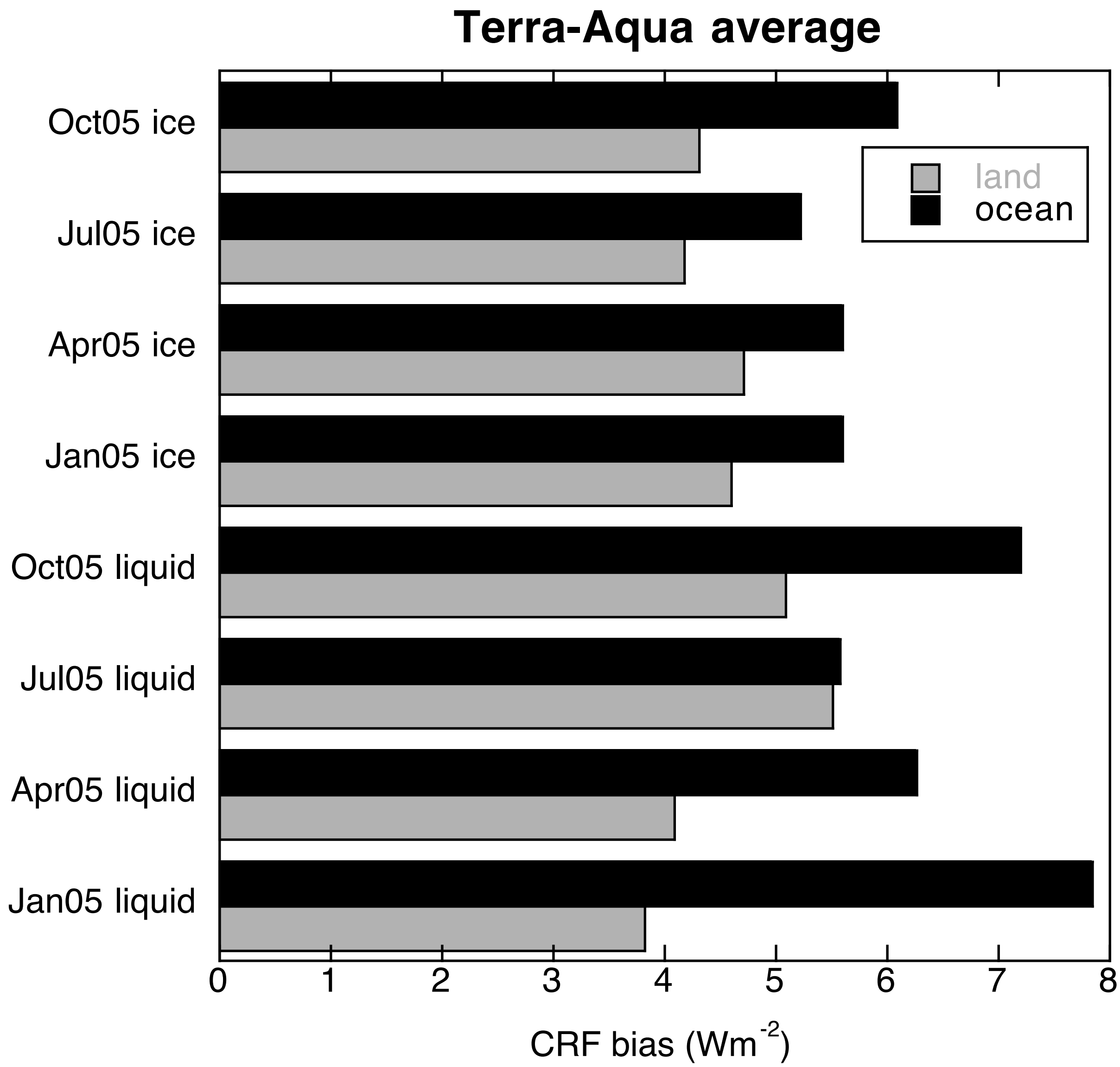

Figure 6. Monthly combined Terra-Aqua B_2^R-based overpass SWCRF bias averaged separately over the globe's land and ocean gridpoints.

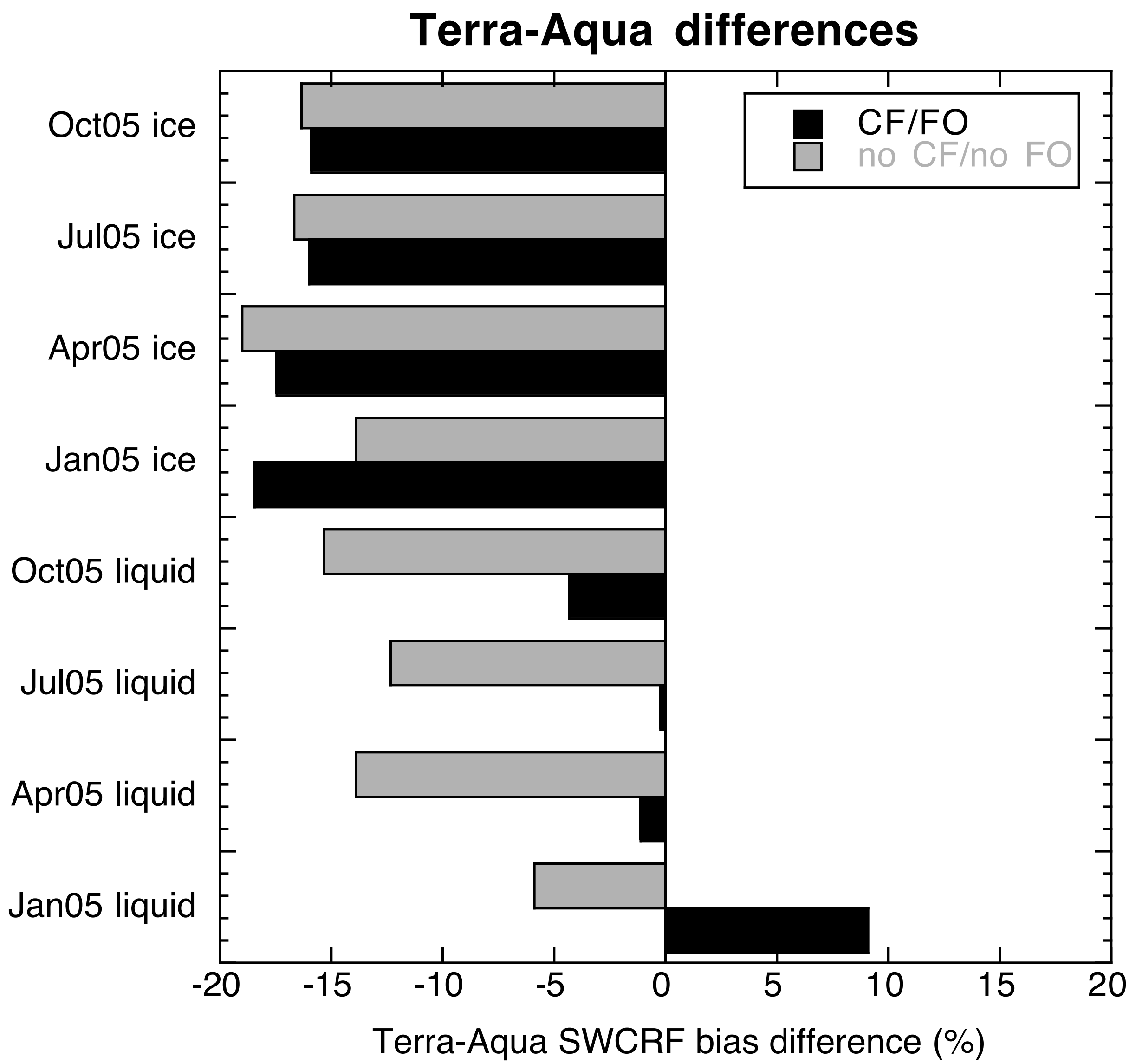

Figure 7. Percentage difference (normalized by their combined value) of Terra minus Aqua global monthly overpass SWCRF biases (B_2^R-based). Along with the default regular SWCRF biases, results from the "no CF/no FO" (see subsection 3c) bias calculation are also shown. These reveal the extent to which the Terra-Aqua SWCRF biases are due to differences in cloud fraction (CF) and frequency of cloud occurrence (FO).

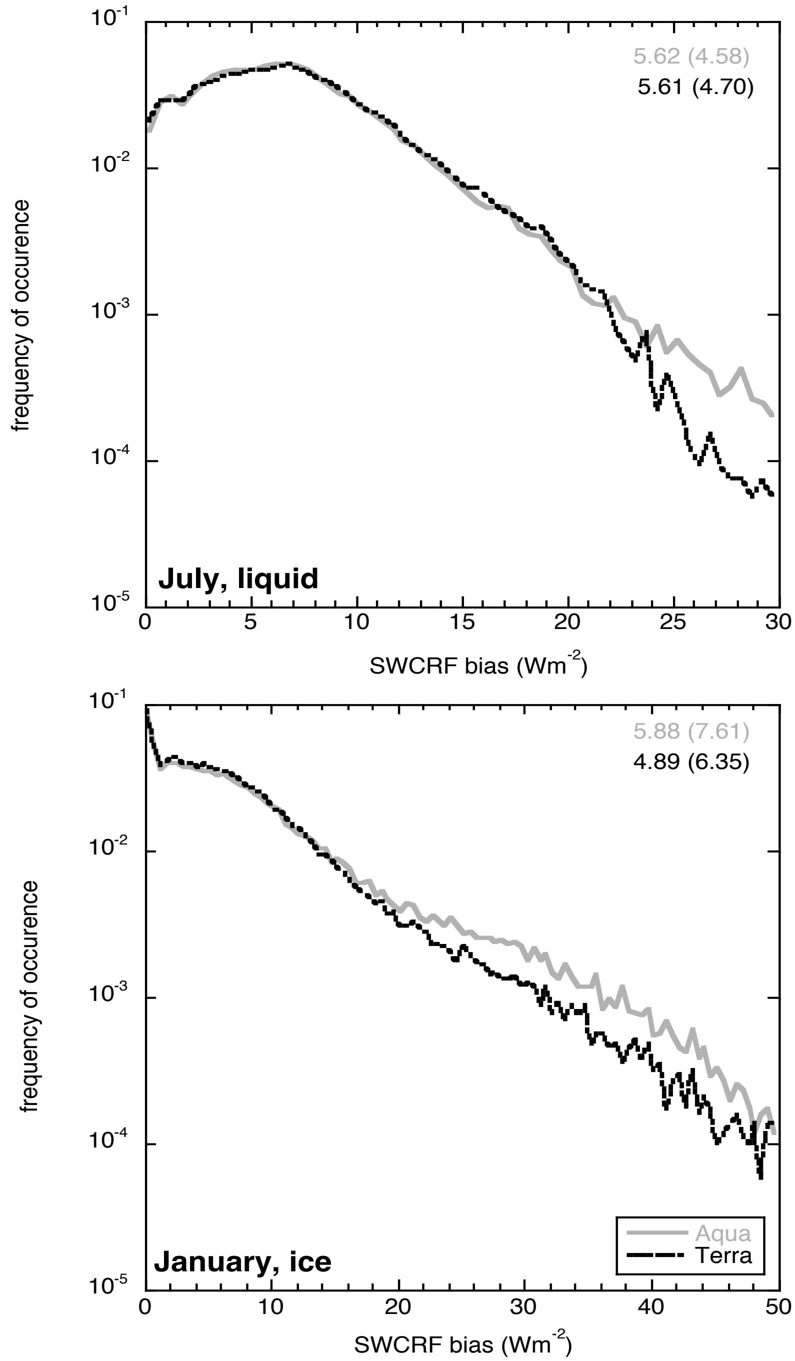

Figure 8. Logarithmic normalized frequency of occurrence of monthly overpass SWCRF biases (B_2^R-based) for July 2005 liquid clouds (top) and January 2005 ice clouds (bottom). The global mean SWCRF biases and their standard deviations (in parentheses) are also given.

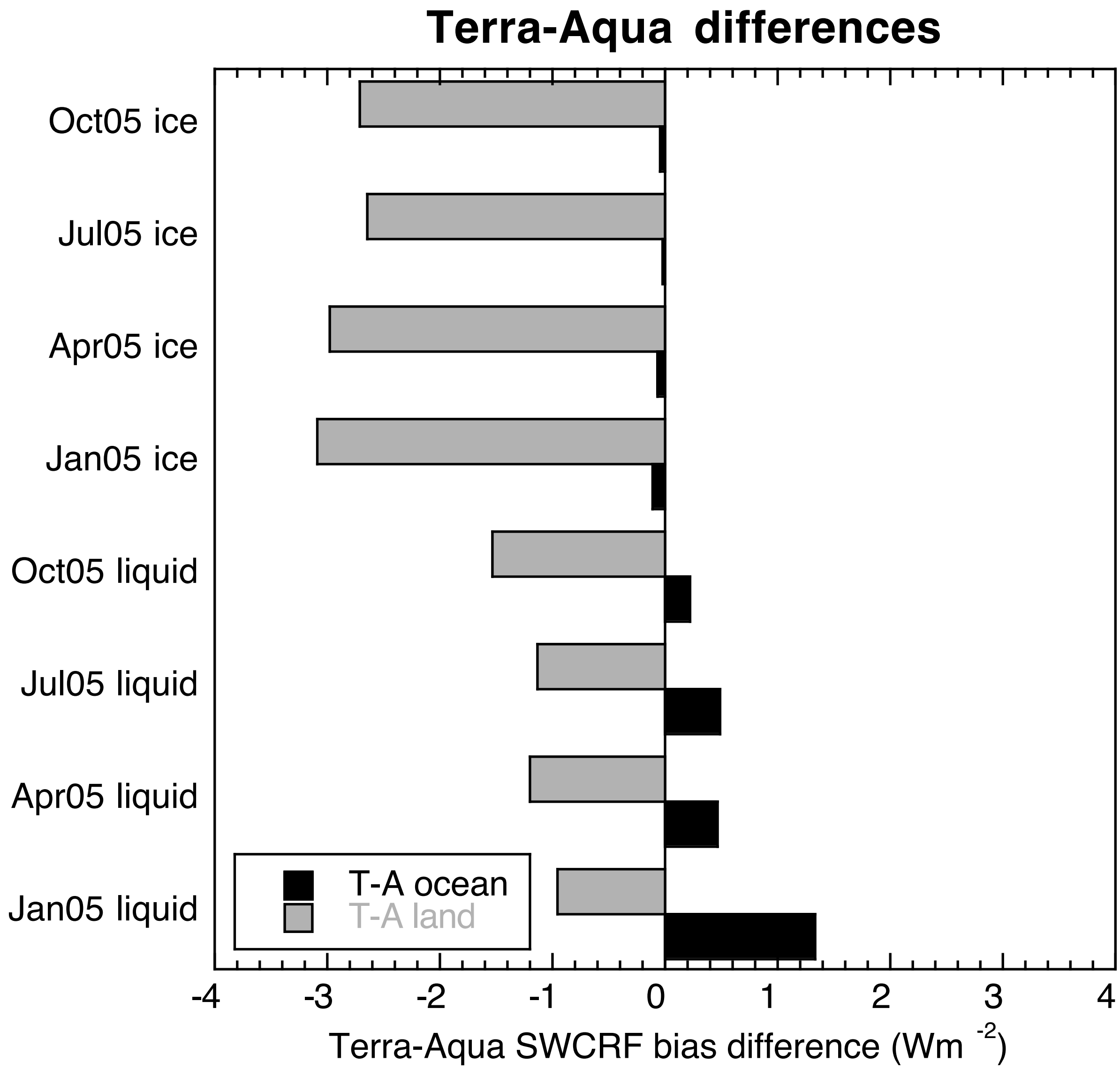

Figure 9. Absolute difference of Terra minus Aqua monthly overpass SWCRF biases (B_2^R-based) averaged separately over the globe's ocean and land gridpoints.